Journal of the European Ceramic Society 40 (2020) 5376–5383

Contents lists available at ScienceDirect

Journal of the European Ceramic Society

journal homepage: www.elsevier.com/locate/jeurceramsoc

Original Article

On the formation mechanism of $Ba_{0.85}Ca_{0.15}Zr_{0.1}Ti_{0.9}O_3$ thin films by aqueous chemical solution deposition

Evgeniya Khomyakova[a], Sigurd Wenner[b], Kristine Bakken[a], Jan Schultheiß[a], Tor Grande[a], Julia Glaum[a], Mari-Ann Einarsrud[a,*]

[a] Department of Materials Science and Engineering, NTNU Norwegian University of Science and Technology, 7491, Trondheim, Norway
[b] SINTEF Industry, Strindvegen 4, 7034, Trondheim, Norway

ARTICLE INFO

Keywords:
Chemical solution deposition
barium calcium zirconium titanate
thin films
crystallization
pyrolysis

ABSTRACT

Here we report on the development of an environmentally friendly, simple and robust aqueous chemical solution route for the fabrication of $Ba_{0.85}Ca_{0.15}Zr_{0.1}Ti_{0.9}O_3$ (BCZT) thin films. Using a stable aqueous precursor solution, thin films were prepared by spin coating and the impact of thermal processing on the microstructure and phase purity of the thin film was revealed by X-ray diffraction and transmission electron microscopy. We find, that barium oxycarbonate formation during the pyrolysis plays a key role in the formation of dense, homogeneous single phase BCZT films. The formation of barium oxycarbonate leads to undesirable segregation of cations, resulting in barium depletion on the BCZT grain boundaries and occurrence of a secondary phase ($CaZrTi_2O_7$). Based on this insight the thermal processing was optimized and dense, oriented and single-phase BCZT films were fabricated by combining a low pyrolysis temperature with rapid heating to the annealing temperature.

1. Introduction

Among promising lead-free ferroelectric materials, the perovskite $(Ba,Ca)(Zr,Ti)O_3$ with the morphotropic phase boundary (MPB) composition $Ba_{0.85}Ca_{0.15}Zr_{0.1}Ti_{0.9}O_3$ (BCZT) possesses the highest piezoelectric response of ~630 pC/N [1–3]. Being non-cytotoxic [4,5] with a low Curie temperature of 80-100 °C [1], BCZT is an ideal candidate for biomedical applications including *in vivo* implants, implantable pressure sensors and hearing aid implants [6,7]. In addition, piezoelectric devices can enable energy harvesting from organ motion creating self-powered pace-makers [8] and promote tissue regeneration by distant, non-evasive stimulation [9]. For these *in vivo* applications, miniature components in the form of thin films are required.

Fabrication of BCZT thin films has been reported using different methods, like pulsed laser deposition [10–12], radio frequency magnetron sputtering [13–15], matrix-assisted pulsed laser evaporation [4], and chemical solution deposition (CSD) [16–29]. CSD is a robust, simple and scalable method that does not require any sophisticated equipment. The preparation of solutions is commonly based on organic solvents. Some approaches have been reported avoiding the use of the toxic 2-methoxyethanol as a solvent, for example by employing acetic acid [16] or a mixture of ethanol, acetic acid and deionized water [17] 17]. Through these routes, thin films with fine, equiaxed grains and different degrees of texturing have been obtained [16–29]. In order to introduce texturing and reduce annealing temperature, different seeding layers have been used, such as $Pb_{0.8}Ca_{0.2}TiO_3$ [21], $Pb_{0.8}Ca_{0.1}La_{0.1}Ti_{0.975}O_3$ [22] and $LaNiO_3$ [23]. The reported piezoelectric properties of CSD-derived BCZT thin films are spread over a wide range [24] with values of the piezoelectric coefficient, d_{33}, ranging from 45 pm/V [24] up to 280 pm/V [19] depending on substrate, electrode material and measurement method.

Knowledge about the phase development from the precursor film to the crystallized film is of utmost importance to obtain thin films of high quality and optimized microstructure. Wang et al. [17]17] provide insight into the reaction mechanism during BCZT thin film fabrication using CSD with acetic acid/alcohol/water as the solvent. They identified $BaCO_3$ and $CaCO_3$ as intermediate phases, while other research groups [18,22,23,27] claim the appearance of a metastable pyrochlore phase.

Here, we report a novel CSD route to phase pure perovskite BCZT thin films. We have developed a simple, robust and environmental-friendly fabrication process using water as the solvent. Through chemical analysis, X-ray diffraction and transmission electron microscopy, we reveal the processes taking place during pyrolysis of the films and towards formation of single phase BCZT. In addition, we discuss the appearance of a metastable, intermediate Ba-oxycarbonate phase

* Corresponding author.
E-mail address: mari-ann.einarsrud@ntnu.no (M.-A. Einarsrud).

https://doi.org/10.1016/j.jeurceramsoc.2020.07.042
Received 22 December 2019; Received in revised form 12 July 2020; Accepted 17 July 2020
Available online 25 July 2020

formed prior to the BCZT perovskite and the simultaneous formation of $CaZrTi_2O_7$. Guided by the knowledge of the phase development as a function of temperature, we optimized the pyrolysis and annealing conditions, which resulted in a preparation route for single phase BCZT films.

2. Materials and Methods

2.1. Solution preparation

The BCZT aqueous solution was prepared from individual solutions of the four cations. The barium precursor solution was prepared using a combination of the two complexing agents ethylenediamintetetraacetate (EDTA) (98.5 %, Sigma Aldrich, USA) and citric acid (CA) (99 %, Sigma Aldrich, USA) as previously developed in our group [28]. EDTA was dissolved in 30 % ammonia solution, then barium nitrate (99.999 %, Sigma Aldrich, USA), CA and deionized water were added to the mixture. The barium to complexing agent ratios Ba:EDTA:CA were 1:1:2. After 30 min of stirring the ammonia solution was added to bring the pH to 8. The titanium precursor solution was derived from titanium (IV) isopropoxide (97.0 %, Sigma Aldrich, USA) dissolved in deionized water. CA was used as complexing agent for Ti with a Ti:CA ratio of 1:3. After stirring for 12 h at 80 °C the solution turned clear. Ammonia solution was added to increase the pH to ~8. Zirconium and calcium solutions were prepared by dissolving $ZrO(NO_3)_2$ (99.0 %, Sigma Aldrich, USA) and $CaNO_3{\cdot}4H_2O$ (99.0 %, Sigma Aldrich, USA) in deionized water.

The concentration of the individual solutions was determined by thermogravimetric analysis before mixing in stoichiometric ratio corresponding to $Ba_{0.85}Ca_{0.15}Zr_{0.1}Ti_{0.9}O_3$. The stable BCZT solution was divided into two parts. One part was concentrated to ~0.3 M by evaporation, while the other part was diluted to ~0.075 M. The solution with ~0.075 M concentration was used for all experiments if not otherwise specified.

2.2. Thin film preparation

Platinized silicon, $Pt/TiO_2/SiO_2/Si$ (Pt/Si) (SINTEF, Oslo, Norway) and $SrTiO_3$ (STO) (Crystal GmbH, Berlin, Germany) were used as substrates. The substrates were plasma cleaned (Femto, Diener Electronic GmbH&Co, Ebhausen, Germany) prior to thin film deposition to improve substrate wetting using oxygen as carrier gas and 1 min of exposition time. The aqueous BCZT solution was spin coated at 3000 rpm for 30 s and then dried on a hot plate at 200 °C for 2 min. After drying, the thin films were heat-treated using an in house developed rapid thermal processing unit with a SiC heater [29]. The rapid heat treatment was conducted in air using several different types of heating profiles (Fig. 1).

In heating profile a) (Fig. 1a)) the as-deposited films were slowly heated to different temperatures for a short holding time and subsequently cooled. Heating profiles b) and c) (Fig. 1b), c)) use the same slow heating ramp to reach an intermediate pyrolysis step, followed by a fast heating ramp to the high temperature annealing step. As the heating profiles b) and c) were applied after each layer deposition, they are referred to as multi-annealing profiles. For heating profile d) (Fig. 1d)) the deposition-drying-pyrolysis cycle was repeated until the desired film thickness was reached, followed by one final annealing step for the whole sample. This heating profile will be referred to as single-annealing profile.

2.3. Characterization

The thin films were characterized by X-ray diffraction (XRD) using a Siemens D5005 high resolution powder diffractometer (Siemens AG, Munich, Germany) with Bragg-Brentano (BB) geometry and a Bruker D8 A25 DaVinci X-ray diffractometer (DaVinci, Karlsruhe, Germany) with grazing incidence (GI) geometry. All XRD analysis was performed with Cu Kα1 radiation.

Scanning electron microscopy (SEM) of the thin film surfaces was performed using a field-emission FE-SEM Zeiss Ultra 55 LE microscope (Carl Zeiss AG, Oberkochen, Germany) with an in-lens detector. Cross sections of the films were obtained by fracturing the samples. No coating was applied to the samples prior to imaging.

Transmission electron microscopy (TEM) specimens were made using a FEI Helios NanoLab DualBeam (Thermo Fisher Scientific, Materials & Structural Analysis Division, Hillsboro, Oregon, USA) focused ion beam (FIB) instrument. The samples were coated with protection layers of Pt and C before cross-sectional specimens were extracted using the Ga ion beam. The specimens were attached to a Cu half-grid and thinned to electron transparency using ion voltages of 30 kV and 5 kV.

TEM/STEM images were obtained with a JEOL ARM-200CF (JEOL Ltd, Akishima, Tokyo, Japan) probe/image-corrected microscope operated at 200 kV. Chemical maps were acquired with a 0.98 Sr Centurio silicon drift detector for energy-dispersive X-ray spectroscopy (EDX), and simultaneously, a GIF Quantum for electron energy-loss spectroscopy (EELS). Typically, we only show EELS maps as the technique gives a higher quality signal than, EDX while otherwise being consistent. The exception is Zr, which did not have a core loss edge in the measured energy loss range. EELS maps are generated by standard power-law background subtraction and edge integration.

3. Results

3.1. XRD analysis of BCZT thin films annealed at different temperatures

The films deposited using 0.3 M solution and annealed at temperatures from 450 to 850 °C via heating profile a) (Fig. 1a)) showed the sequence of phase formation and identified that intermediate phases appeared during the heat treatment. BB XRD diffractograms of these films annealed at 450 and 500 °C show only diffraction lines of the substrate, meaning that the deposited film is still amorphous (Fig. 2a). Crystallization of the perovskite phase begins at 550 °C with an intermediate phase present as signified by a diffraction line at 26.7°. After

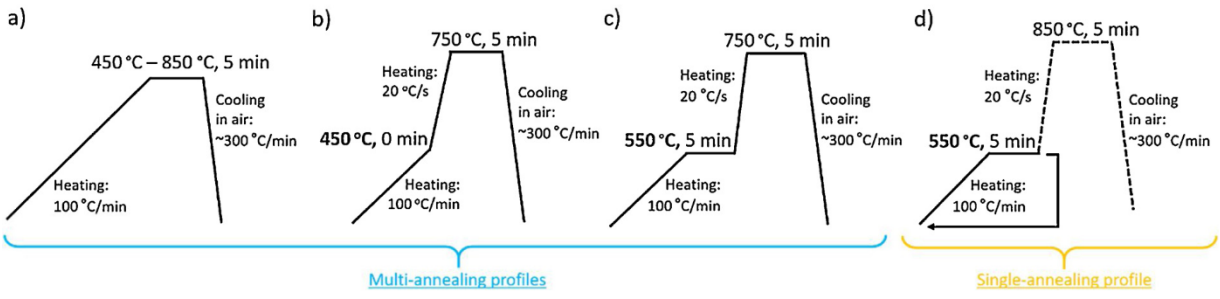

Fig. 1. Schematic illustrations of a)-c) multi-annealing and d) single-annealing heating profiles used for BCZT thin film pyrolysis and annealing.

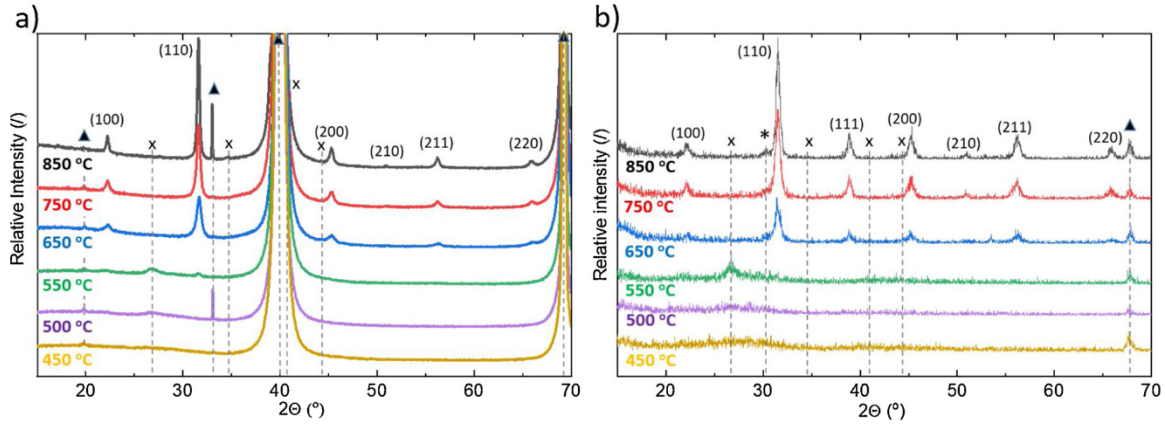

Fig. 2. BB (a) and GI (b) XRD patterns of BCZT/Pt/Si thin films annealed at different temperatures. ▲: substrate; (hkl): BCZT (PDF: 04-019-9414); x: Ba-oxycarbonate; *: $CaZrTi_2O_7$ (PDF: 04-007-6894).

treatment at temperatures above 550 °C only diffraction lines of BCZT are observed. These results are in accordance with the XRD patterns of solution-derived BCZT powders calcined at the same temperatures (See Supplementary Information Fig. S1).

The intermediate phase, marked with "x" in Fig. 2 and supplementary Fig. S1, with diffraction lines observed both in thin films (Fig. 2) and powders (Fig. S1) annealed at 550 °C, is proposed to be a Ba-oxycarbonate phase previously observed during sol-gel synthesis of $BaTiO_3$ [30–34]. Formation of an intermediate metastable Ba-oxycarbonate phase and Ba-deficient barium titanates has been reported prior to crystallization of $BaTiO_3$ [30–34]. However, in the case of BCZT, the exact composition of the oxycarbonate phase may be different from the one reported for $BaTiO_3$ as some Ca might be dissolved. Hence, the suggested formation of pyrochlore [18,22,23,27,35] or barium carbonate [17]17] during synthesis of BCZT could as well be an Ba,Ca-oxycarbonate phase.

According to BB XRD (Fig. 2 a)), the thin films annealed at 650, 750, and 850 °C are single phase, polycrystalline BCZT with randomly oriented grain structure. With increasing annealing temperature, BCZT perovskite diffraction lines become sharper, reflecting the higher degree of crystallinity. On the other hand, the GI patterns of the same thin films (Fig. 2 b)) show a diffraction line marked with *, which reveals a small amount of a $CaZrTi_2O_7$ secondary phase ((PDF: 04-007-6894), as will be shown in more details later. In GI geometry, a larger volume fraction of the film is probed compared to BB configuration, such that small amounts of secondary phases become detectable.

The appearance of the secondary phase is dependent on the pyrolysis conditions. GI XRD of two BCZT thin films fabricated in the same way but with different pyrolysis steps (heating profiles b) and c) in Fig.1) are shown in Fig. 3. The thin film pyrolyzed using heating profile b) (450 °C for 0 min) results in single phase BCZT, while a low intensity diffraction line at ~30.5° attributed to $CaZrTi_2O_7$ is evident in the diffractogram of the films pyrolyzed according to heating profile c) (550 °C for 5 min).

3.2. TEM analysis of the BCZT thin film pyrolyzed at 550 °C

The effect of the pyrolysis conditions was thoroughly investigated by studying a BCZT film composed of 20 layers, which was pyrolyzed at 550 °C after each layer, but not subjected to the final annealing step. The bright field (BF) TEM image of the film (Fig. 4 a)) demonstrates that the ~280 nm thick film consists of three distinct regions with different morphologies. The top region with a thickness of ~130 nm is characterized by some porosity (pores marked by arrows) and low crystallinity. The presence of an amorphous phase can be seen from the selected area electron diffraction (SAED) pattern (Fig. 4 b)) as a broad, diffuse ring located between the simulated (001) and (011) perovskite

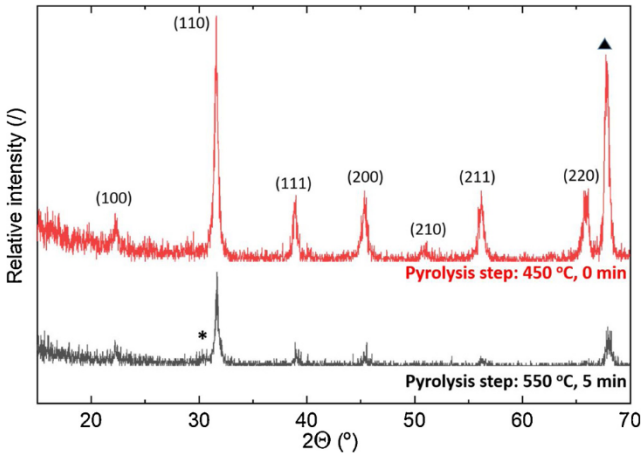

Fig. 3. GI XRD patterns of BCZT/Pt/Si thin films pyrolyzed at different conditions and multi-annealed at 750 °C (heating profiles b) and c) in Fig. 1b,c). ▲: substrate; (hkl): BCZT (PDF: 04-019-9414); *: $CaZrTi_2O_7$ (PDF: 04-007-6894).

diffraction rings. The middle region is characterized by a high degree of porosity with homogeneously distributed small, round pores. Similar to the top region, the middle region exhibits low crystallinity (Fig. 4 c)). In great contrast, the bottom region is highly crystalline, as signified by the pronounced reflections in the SAED pattern, with only a small amount of amorphous phase remaining (Fig. 4 d)). The bottom region is denser (pores marked by arrows) than the middle region, but possesses larger pores concentrated predominantly at the interface with Pt. The bottom and medium regions have about the same thickness (~70 nm). Together with the SAED patterns, the large difference in crystallinity between the three regions is demonstrated in the dark field (DF) TEM image (Fig. 4 e)), where crystalline grains with certain orientations appear with bright contrast.

The phase composition of the pyrolyzed BCZT films also changed from the bottom to the top. Superimposed on the experimental SAED patterns (Fig. 4 b)-d)) are simulated patterns for polycrystalline BCZT (red circles each marked with hkl indexes) as observed in the XRD patterns (Figs. 2 and 3). For the middle and bottom regions, the simulated patterns match the experimentally recorded SAED patterns well (Fig. 4 c) and d)). In the pattern of the top region (Fig. 4 b)) two distinct circles are observed (marked by blue circle and arrows). Their d-spacings of 0.410 and 0.330 nm are in good accordance with the oxycarbonate phase reflections at 21.6 and 26.7° in the XRD patterns of BCZT thin films and powders annealed at 550 °C (Fig. 2 and Fig. S1). In addition, the diffuse low intensity rings also present in the SAED patterns of the middle and bottom regions (Fig. 4 c), d)) have the same d-

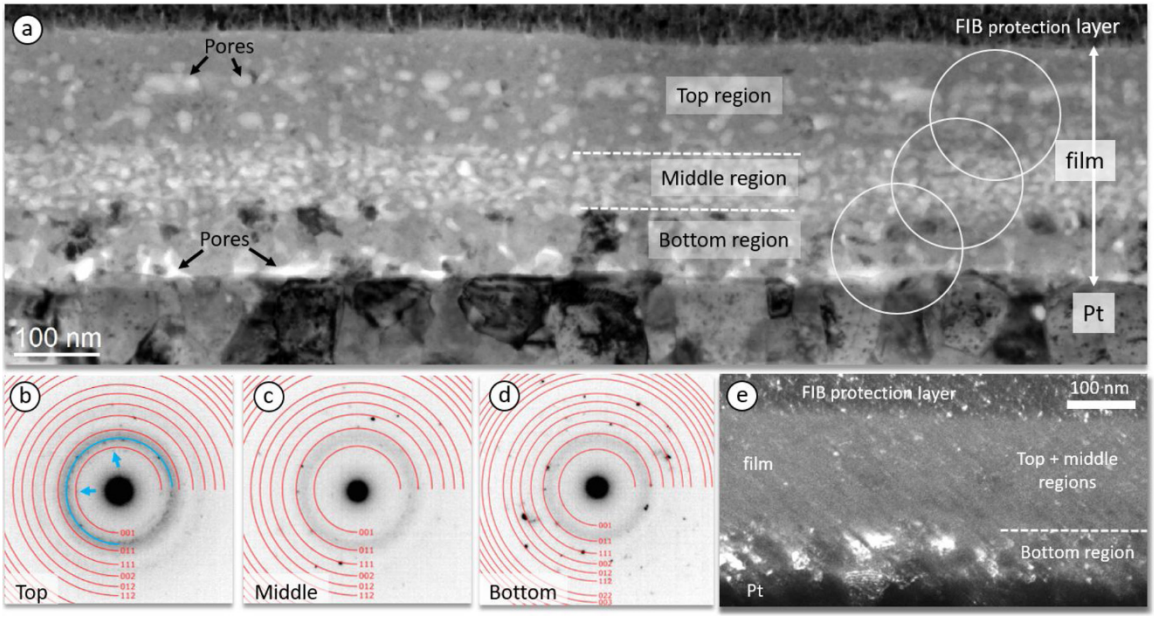

Fig. 4. BF TEM image (a), SAED patterns from corresponding thin film areas (b-d), DF TEM image (e) of the BCZT/Pt/Si films with each of the 20 layers pyrolyzed at 550 °C for 5 min.

spacing of 0.330 nm, which indicates the presence of small amounts of the oxycarbonate phase.

The element distribution throughout the cross-section of the BCZT thin film is presented in Fig. 5 as annual dark field scanning TEM (ADF-STEM) image (Fig. 5 a), EELS element mappings (Fig. 5 b) – f)) and integrated line profiles (Fig. 5 g)). The carbon distribution in the BCZT film was thoroughly investigated by EELS (Figs. 5 b), g)) as it is a key to follow the development of the oxycarbonate phase. The carbon content is highest in the top region and gradually decreases towards almost zero at the film/substrate interface. The gradual reduction in carbon content shows that the oxycarbonate phase decomposes continuously, proportional to the time spent at the pyrolysis temperature.

An overall homogeneous distribution of the elements Ca, Ba, Zr, and Ti was noticed in the top region of the samples (Figs. 5 c) – g)). However, on the local scale a core-shell structure with Ba depletion at the at the grain-pore interfaces and Ba enrichment of the grain interior is observed. The middle region exhibits pronounced depletion in Ba and weak depletion in Ca compared to the top region, as demonstrated by the Ba and Ca integrated intensity profiles (Fig. 5 g)). In addition, depletion of Ba on the grain surface/boundaries becomes more obvious in the middle region (insets on Figs. 5 c), d), e)).

3.3. TEM analysis of BCZT films pyrolyzed at 550 °C and annealed at 850 °C

A similar BCZT film, as presented in Figs. 4 and 5, was further annealed at 850 °C for 5 min, such that total heat treatment was made according to heating profile d) (Fig. 1). In addition to BCZT films on silicon substrate, a BCZT thin film on STO substrate subjected to the same heating profile was analyzed. Both films showed the presence of

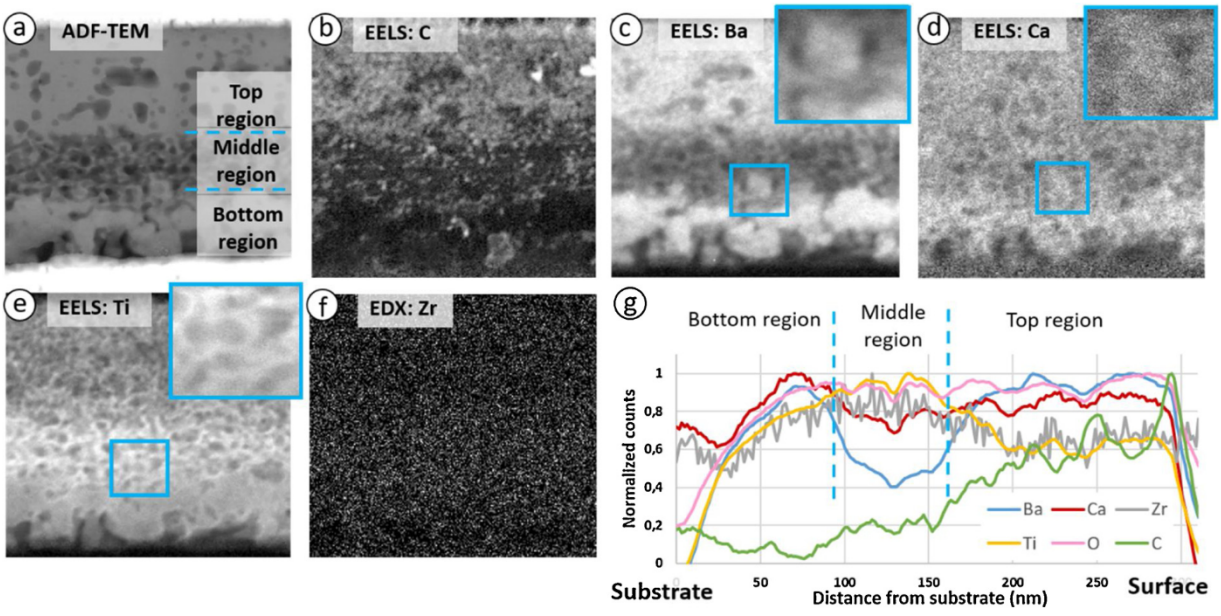

Fig. 5. ADF-STEM image (a), EDX/EELS mappings (b-f) and integrated line profiles (g) of BCZT/Pt/Si film with each layer pyrolyzed at 550 °C for 5 min.

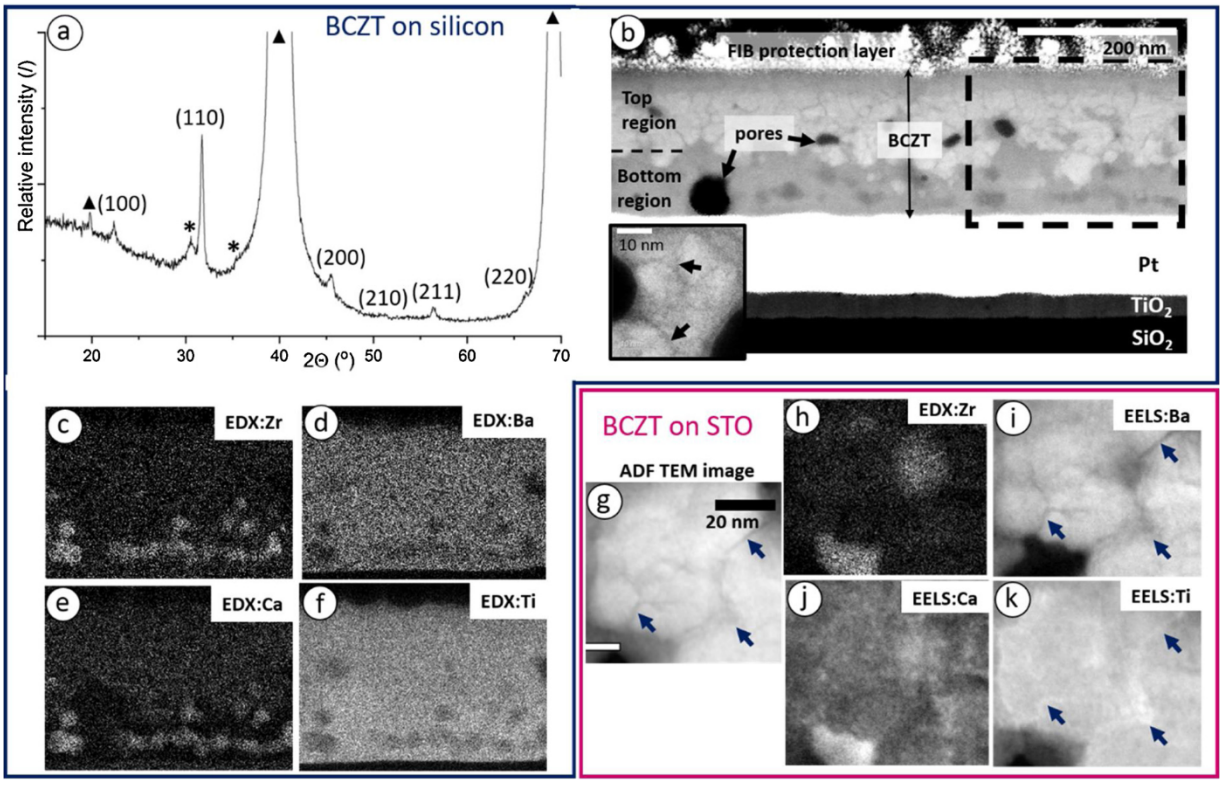

Fig. 6. BCZT/Pt/Si films: XRD (a), ADF-STEM image (b), EDX (c-f) mappings taken from the hatched area in (b). Inset in (b) is taken from top region of the film. BCZT/STO film: ADF-STEM image (g) and EDX/EELS (h-k) mappings. Both thin films were annealed up to 850 °C in the same way (heating profile d). ▲: substrate; (hkl): BCZT phase (PDF: 04-019-9414); *: $CaZrTi_2O_7$ (PDF: 04-007-6894).

$CaZrTi_2O_7$ as evidenced by TEM analysis. Complete analyses of these films are presented in Fig. 6.

3.4. Annealed film on silicon substrate

BB XRD pattern of the film on silicon substrate (Fig. 6 a)) exhibits strong reflections of the perovskite phase together with distinct reflections of the $CaZrTi_2O_7$ phase. The amount of this secondary phase is significantly larger compared to the film presented in Fig. 2, which was annealed at the same temperature, but did not undergo repeated pyrolysis (heating profile a) in Fig. 1). This clearly highlights the importance of the heating profile and especially the pyrolysis step on the phase purity of the final films.

The ADF TEM image (Fig. 6 b)) shows that the thickness of the film annealed to 850 °C is ~200 nm, which is ~80 nm thinner compared to the only pyrolyzed film (Fig. 4 a)). Hence, significant densification occurred during the high temperature annealing with only a few pores remaining (marked by arrows in Fig. 6 b)). The porous middle region observed after the pyrolysis step is no longer visible and the annealed film consists of two regions with clear difference in phase composition.

According to the EDX mappings (Figs. 6 c) - f)) conducted in the dashed rectangular area in Fig. 6 b), the upper region exhibits a homogeneous distribution of all elements. The bottom region, however, contains ~30 nm-sized round inclusions of a secondary phase, which is enriched in Zr and Ca (Figs. 6 c), e)). The EELS analysis of the Ca,Zr-rich secondary phase (Fig. 6 g) -k)) demonstrates that the phase does not contain Ba (Fig. 6 i)), however, it contains Ti (Fig. 6 k)). This supports the observation of a $CaZrTi_2O_7$ phase in the XRD data (Figs. 2, 3 and 6a) and is in accordance with the EDX mapping in Figs. 6 e) and f), where the EDX signal of both Ba and Ti is much weaker in the areas of the secondary phase.

3.5. Annealed film on STO substrate

Analyzing the BCZT thin film on an STO substrate, another interesting feature was noticed. While EDX/EELS analysis revealed that the film exhibits an overall homogeneous distribution of the elements (overall mappings not shown) resulting in a BCZT film with inclusions of Ca,Zr-rich secondary phase, distinct inhomogeneities were observed on the local scale. At the grain boundaries, the signal from Ba is reduced, whereas the signal from Ti is increased. (Figs. 6 i) and k) marked by arrows). The ADF image of the EELS mapped area also exhibits lower intensity at the grain boundaries (Fig. 6 g), marked by arrows), suggesting the presence of a lower-mass element.

The Ba EELS map (Fig. 6 i)) coupled with the ADF image (Fig. 6 g)) observed through the whole BCZT layer on STO substrate suggests that the depletion of Ba at the grain boundaries happens through the whole top region in the film on silicon substrate as well (Fig. 6 b) and inset, marked by arrows). It is important to note, that the depletion of Ba at the grain-pore boundaries as observed for the pyrolyzed sample (Figs. 5 c), e) and insets) persists even after annealing at 850 °C (Figs. 6 b), g), i)).

3.6. TEM analysis of the single phase BCZT films

In contrast to the BCZT film pyrolyzed at 550 °C, a lower pyrolysis temperature of 450 °C results in a single-phase film (Fig. 3). The ADF-STEM image of a film pyrolyzed at 450 °C (Fig. 7 a)) shows a dense, homogeneous, single phase BCZT film with only a few pores (marked by arrows). High density of the film is also confirmed by the SEM image (Fig. S2), showing a broad grain size distribution with grains in the range from 10 to 190 nm. It should be noted that this range falls into the range of critical grain size reported for BT ceramics below which the crystal structure approaches centrosymmetric symmetry and the ferroelectric response is reduced [36,37]. The polarization-electric field

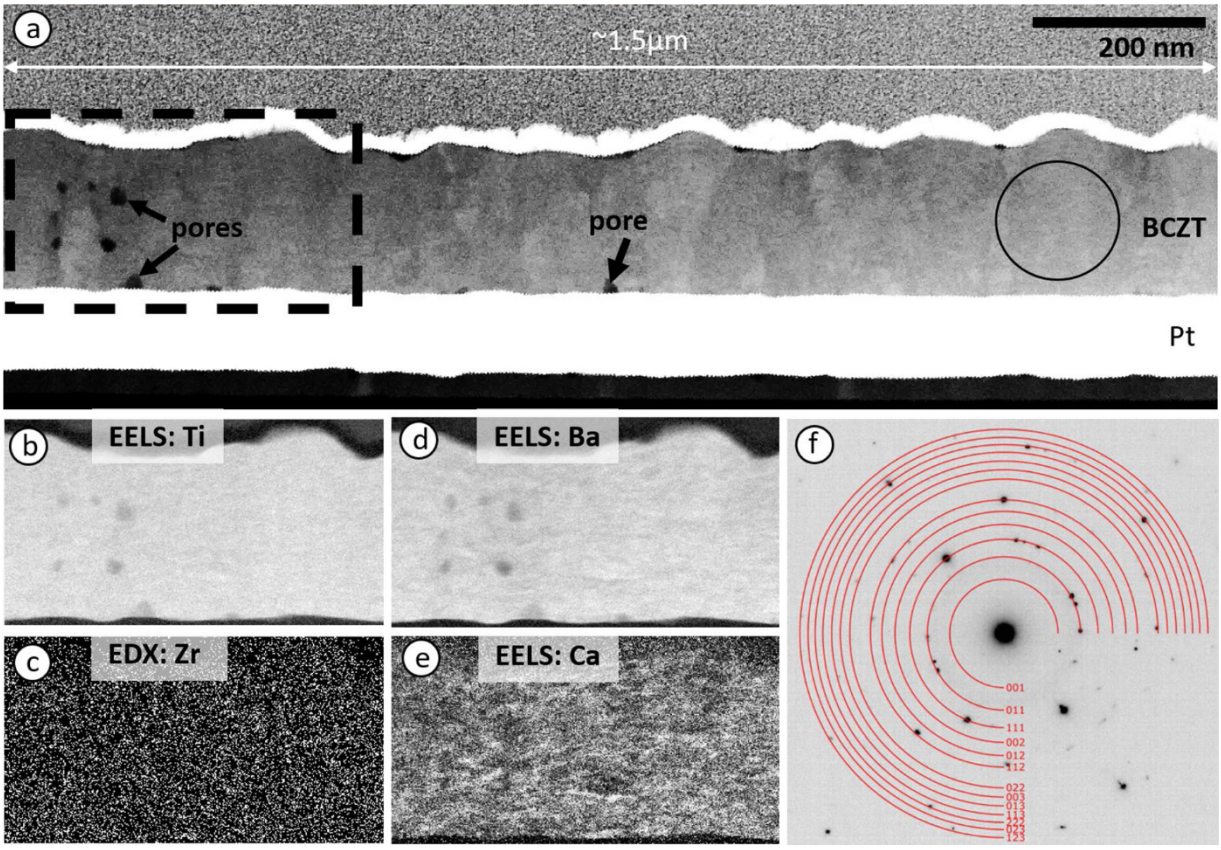

Fig. 7. Single phase BCZT thin film (heating profile b), ADF-STEM (a), EELS of Ti (b), EDX of Zr (c), EELS of Ba (d), EELS of Ca (e) mappings and SAED (f) from the area marked by the circle in a).

response given ins Figure S4 indicates that this mechanism might be of relevance for the present sample. The EDX/EELS mappings (Fig. 7 b) – e)) taken from the hatched areas in Fig. 7 a) prove a homogeneous distribution of the elements throughout the whole film and no depletion of Ba between the grains or at the grain-pore boundaries is observed. Furthermore, the experimental SAED pattern taken from the circled area on Fig. 7 a) is perfectly indexed by the simulated perovskite phase (Fig. 7 f)).

4. Discussion

We have shown that the pyrolysis conditions are the key factor in the preparation of single phase BCZT films by water-based CSD. Various processes take place in the film already during the pyrolysis enhancing or suppressing element segregation and the formation of secondary phases. The BCZT thin film composed of 20 subsequently pyrolyzed layers illustrates the sequence of processes that occur during the pyrolysis stage (Figs. 4 and 5). The top region of the film corresponds to short term exposure (up to 25 min) at 550 °C, while the bottom region corresponds to long-term heating (up to 100 min). Both regions exhibit significant differences in morphology, crystallinity and phase composition, which is schematically shown in Fig. 8.

When the as-spun film is pyrolysed, decomposition of the organic precursors and nitrates takes place releasing CO_2 and leading to the formation of an amorphous film (Fig. 2), This is illustrated in scheme A of Fig. 8. Pyrolysis of the amorphous film at 550 °C initiates the formation of the intermediate oxycarbonate phase (Figs. 2,4 a), 4 b) and 5) as shown in scheme B of Fig. 8.

In the BCZT system, however, both Ca and Ba may react with CO_2 to form various carbonates, i.e. $BaCO_3$ or $(Ba,Ca)(CO_3)_2$, as shown in supplementary Fig. S1. Hence, Ca may participate in the formation of the oxycarbonate phase and we will use a general formula for the oxycarbonate phase in the BCZT system in the following. We propose that in the early stage of pyrolysis a Ba,Ca-oxycarbonate phase and its Ba,Ca-depleted BCZT counterpart forms, similar to the reaction proposed by Ischenko et al. for $BaTiO_3$ thin films [32,33]:

$$(1)\ (Ba,Ca,Ti,Zr) - \text{precursor complex} \rightarrow (1 - y)(Ba,Ca)O_x(CO_3)_{1-x} + (Ba,Ca)_y(Ti,Zr)O_{2+y}$$

The oxycarbonate phase forms dispersed nanoparticles, while the Ba,Ca-depleted BCZT is observed as core-shell structures (Figs. 5 c) – e) and insets) where especially Ba-deficiency is observed at the particles surface, creating the top region in Fig. 4 and 5. The high amount of carbon in the top region (Figs. 4 b) and 5 b)) confirms the high concentration of the oxycarbonate phase. As the oxycarbonate phase is metastable, it gradually decomposes if the sample is kept at 550 °C for longer time, thus reducing the amount of carbon (Fig. 5 b), g)). Eventually, the two phases formed in reaction (1) will react to stoichiometric BCZT (Fig. 4,5) if the reaction is not kinetically hindered.

Decomposition of the major fraction of organic phase occurs in the temperature range from 200 to 550 °C (thermal analysis results shown in Fig. S3) providing an atmosphere locally enriched with CO_2 from each newly deposited layer. The emission of CO_2 is illustrated in the schemes B, C and D in the Fig. 8 by grey arrows. During the pyrolysis of a newly deposited layer, oxycarbonate is formed by reaction (1). Decomposition of this oxycarbonate phase requires a heat treatment of the film at 550 °C for longer time (Fig. 4 and 5), while more and more layers being deposited on the top. Hence, the oxycarbonate phase decomposing continuously emits CO_2 from the deposited layers, keeping the atmosphere locally enriched with CO_2 for a longer time.

The enrichment of the atmosphere with CO_2 leads to the stabilization and growth of the Ba,Ca-oxycarbonate crystals on the film surface and hence the formation of a Ba-depleted BCZT surface/grain boundaries as is also shown by Sazinas et al. [38]. In the similar way reported

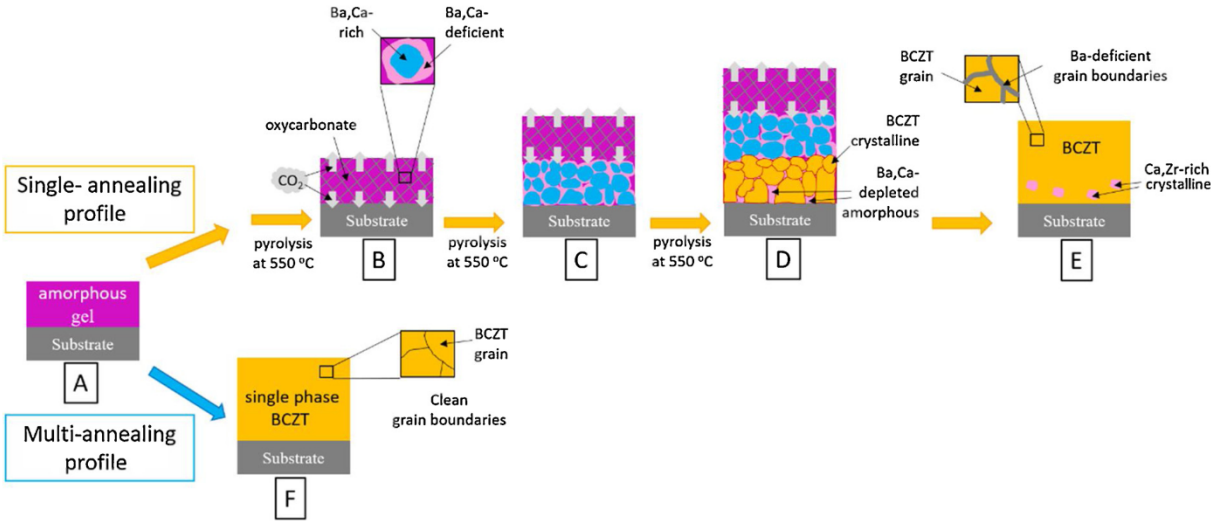

Fig. 8. Schematic representation of phase formation and crystallization of the perovskite BCZT thin films.

in [38], BCZT and/or $(Ba,Ca)_y(Ti,Zr)O_{2+y}$ phase formed in reaction (1) may react further with CO_2 enhancing the initial Ba,Ca-depletion. This process is illustrated in the schemes B and C in Fig. 8.

The formed Ba,Ca-oxycarbonate phase and Ba,Ca-depleted phase will react during prolonged pyrolysis at 550 °C as is evidenced from Figs. 4 and 5. The reaction is kinetically hindered due to long diffusion distances and low reaction temperature, resulting in the residual presence of a Ba,Ca-depleted amorphous phase and Ba,Ca-enriched perovskite BCZT (scheme D of Fig. 8). Once the cations are separated by the formation of the two phases, complete reaction to BCZT is very slow even by high-temperature annealing, (Fig. 6) due to the low diffusion coefficients of Ba and Zr [39]. Sazinas et al. reported the diffusion coefficient of Ba to be several orders of magnitude higher than for Zr, explaining the mobility of Ba [39]. Ba diffusion is also reported to be faster in $BaTiO_3$ compared to $BaZrO_3$ [40]. During the high temperature annealing step, the Ba,Ca-depleted amorphous phase crystallize into a Ca,Zr rich secondary phase located close to the BCZT/Pt interface (Figs. 6 b) -f), scheme E in Fig. 8), which is in accordance with the proposed hypothesis. The reaction is more complete at the interface to the substrate, as the first deposited layers have spent the longest time at 550 °C. Moreover, the Ba depleted shell of the particles formed during the pyrolysis step (Figs. 5 c) – e), scheme B in Fig. 8), is not eliminated by high temperature annealing, but results in Ba-depleted grain boundaries (Figs. 6 b), g), i), k), scheme E in Fig. 8).

The undesired cation segregation and formation of secondary phase, which appears at ~550 °C, is based on the high stability of the Ba,Ca-carbonate, particularly at high Ba-content. The formation of this phase can be avoided, if a lower pyrolysis temperature is utilized, followed by very fast heating to the annealing temperature, where formation of the single-phase perovskite BCZT film takes place (Fig. 7, scheme F in Fig. 8). This highlights that controlling the processes taking place during the pyrolysis step is the key to obtain single-phase BCZT thin films with a homogeneous microstructure. From this stage, the next steps should include careful analysis of the piezoelectric performance and its optimization e.g. through controlled growth of the average grain size and tailoring of the ionic defects present in the material. Similar reaction schemes as revealed here are expected to occur during deposition of thin films of other complex oxides especially containing basic cations like Ca, Sr and Ba, hence the reaction mechanism determined will aid the optimization of thin oxide film chemical solution deposition also of these materials.

5. Conclusion

In summary, BCZT thin films on platinized silicon and STO substrates were fabricated by aqueous CSD method, i.e. through a simple, economic, robust and environmental-friendly synthesis. We demonstrated that pyrolysis conditions are the key parameters in preparation of single phase BCZT thin films. By using chemical mapping, imaging and diffraction analysis in a TEM, as well as XRD we revealed the mechanisms governing the film formation during the pyrolysis step. Formation of a metastable Ba,Ca-oxycarbonate intermediate phase during the pyrolysis was shown to be the critical step leading to element separation and consequent formation of a secondary $CaZrTi_2O_7$ phase along with perovskite BCZT. Based on the knowledge of the phase development we demonstrated optimized pyrolysis and annealing conditions by combining a low pyrolysis temperature with rapid heating to the annealing temperature hinder the formation of the Ba,Ca-oxycarbonate phase, resulting in the formation of single phase BCZT films.

Declaration of Competing Interest

The authors declare that they have no known competing financial interests or personal relationships that could have appeared to influence the work reported in this paper.

Declaration of Competing Interest

The authors report no declarations of interest.

Acknowledgement

The Research Council of Norway is acknowledged for the financial support through Nano2021 PIEZOMED project number 250184, support to the Norwegian Micro- and Nano-Fabrication Facility, NorFab, project number 245963/F50. J.S. acknowledges the support of the Alexander von Humboldt Foundation through the Feodor-Lynen fellowship. The TEM work was carried out on the NORTEM (NFR grant 197405) infrastructure at the TEM Gemini Centre, Trondheim, Norway. Dr Anders B. Blichfeld is acknowledged for the help and advice concerning the use of the rapid thermal processing unit. Prof. Dr. D. Meier is acknowledged for helpful discussions.

Appendix A. Supplementary data

Supplementary material related to this article can be found, in the

online version, at doi:https://doi.org/10.1016/j.jeurceramsoc.2020.07.042.

References

[1] J. Rödel, K.D. Webber, R. Dittmer, W. Jo, M. Kimura, D. Damjanovic, "Transferring lead-free piezoelectric ceramics into application", J. Eur. Ceram. Soc. 35 (2015) 1659–1681.

[2] J. Gao, D. Xue, W. Liu, Ch. Zhou, X. Ren, Recent Progress on $BaTiO_3$-based piezoelectric ceramics for actuator applications, Actuators 6 (2017) 24.

[3] M. Acosta, N. Novak, V. Rojas, S. Patel, R. Vaish, J. Koruza, G.A. Rossetti, J. Rödel, $BaTiO_3$-based piezoelectrics: fundamentals, current status, and perspectives, Appl. Phys. Rev. 4 (2017) 041305.

[4] N.D. Scarisoreanu, F. Craciun, V. Ion, R. Birjega, A. Bercea, V. Dinca, M. Dinescu, L.E. Sima, M. Icriverzi, A. Roseanu, L. Gruionu, G. Gruionu, Lead-Free piezoelectric (Ba,Ca)(Zr,Ti)O_3 thin films for biocompatible and flexible devices, ACS Appl. Mater. Interfaces 9 (2017) 266–278.

[5] K.K. Poon, M. Wurm, D.M. Evans, M.-A. Einarsrud, R. Lutz, J. Glaum, Biocompatibility of (Ba,Ca)(Zr,Ti)O_3 piezoelectric ceramics for bone replacement materials, J. Biomed. Mater. Res. Part B 108B (2020) 1295–1303.

[6] G.-T. Hwang, M. Byun, C.K. Jeong, K.J. Lee, Flexible piezoelectric thin-film energy harvesters and nanosensors for biomedical applications, Adv. Healthcare Mater. 4 (2014) 646–658.

[7] P. Bingger, J. Fiala, A. Seifert, N. Weber, A. Moser, F. Goldschmidtboeing, K. Foerster, C. Heilmann, F. Beyersdorf, P. Woias, H. Zappe, Implantable multi sensor system for in vivo monitoring of cardiovascular parameters, Transducers 2009-2009 International Solid-State Sensors, Actuators and Microsystems Conference, Denver, USA, 2009, pp. 1469–1472.

[8] C. Dagdeviren, B.D. Yang, Y. Su, P.L. Tran, P. Joe, E. Anderson, J. Xia, V. Doraiswamy, B. Dehdashti, X. Feng, B. Lu, R. Poston, Z. Khalpey, R. Ghaffari, Y. Huang, M.J. Slepian, J.A. Rogers, Conformal piezoelectric energy harvesting and storage from motions of the heart, lung, and diaphragm, PNAS 5 (2014) 1927–1932.

[9] A. Marino, G.G. Genchi, E. Sinibaldi, G. Ciofani, Piezoelectric effects of materials on bio-interfaces, ACS Appl. Mater. Interfaces 9 (2017) 17663–17680.

[10] N.D. Scarisoreanu, F. Craciun, A. Moldovan, V. Ion, R. Birjega, C. Ghica, R.F. Negrea, M. Dinescu, High permittivity $(1-x)Ba(Zr_{0.2}Ti_{0.8})O_3-x(Ba_{0.7}Ca_{0.3})TiO_3$ ($x = 0.45$) epitaxial thin films with nanoscale phase fluctuations, ACS Appl. Mater. Interfaces 7 (2015) 23984–23992.

[11] Q. Lin, D. Wang, S. Li, Strong effect of oxygen partial pressure on electrical properties of $0.5Ba(Zr_{0.2}Ti_{0.8})O_3$–$0.5(Ba_{0.7}Ca_{0.3})TiO_3$ Thin Films, J. Am. Ceram. Soc. 98 (2015) 2094–2098.

[12] W.L. Li, T.D. Zhang, Y.F. Hou, Y. Zhao, D. Xu, W.P. Cao, W.D. Fei, Giant piezoelectric properties of BZT–0.5BCT thin films induced by nanodomain structure, RSC Adv. 4 (2014) 56933–56937.

[13] B.C. Luo, D.Y. Wang, M.M. Duan, S. Li, Orientation-dependent piezoelectric properties in lead-free epitaxial $0.5BaZr_{0.2}Ti_{0.8}O_3$-$0.5Ba_{0.7}Ca_{0.3}TiO_3$ thin films, Appl. Phys. Lett. 103 (2013) 122903.

[14] Y. Han, Z. Zhang, F. Wang, K. Zhang, Piezoelectric properties of bilayer ferroelectric thin films based on $(1-x)Ba(Zr_{0.2}Ti_{0.8})O_3$ –$x(Ba_{0.7}Ca_{0.3}TiO_3)$, Mater. Lett. 177 (2016) 68–70.

[15] B.C. Luo, D.Y. Wang, M.M. Du, S. Li, Growth and characterization of lead-free piezoelectric $BaZr_{0.2}Ti_{0.8}O_3$–$Ba_{0.7}Ca_{0.3}TiO_3$ thin films on Si substrates, Appl. Surf. Sci. 270 (2013) 377–381.

[16] W. Li, J. Hao, H. Zeng, J. Zhai, Dielectric and piezoelectric properties of the $Ba_{0.92}Ca_{0.08}Ti_{0.95}Zr_{0.05}O_3$ thin films grown on different substrate, Curr. Appl. Phys. 13 (2013) 1205–1208.

[17] Z.-M. Wang, K. Zhao, X.-L. Guo, W. Sun, H.-L. Jiang, X.-G. Han, Xu-T. Tao, Z.-X. Cheng, H.-Y. Zhao, H. Kimura, G.-L. Yuan, J. Yin, Z.-G. Liu, Crystallization, phase evolution and ferroelectric properties of sol-gel-synthesized $Ba(Ti_{0.8}Zr_{0.2})O_3$- $x(Ba_{0.7}Ca_{0.3})TiO_3$ thin films, J. Mater. Chem. C 1 (2013) 522–530.

[18] G. Kang, K. Yao, J. Wang, $(1-x)Ba(Zr_{0.2}Ti_{0.8})O_3$–$x(Ba_{0.7}Ca_{0.3})TiO_3$ ferroelectric thin films prepared from chemical solutions, J. Am. Ceram. Soc. 95 (2012) 986–991.

[19] L. Huang, Y. Dai, Y. Wu, X. Pei, W. Chen, Enhanced ferroelectric and piezoelectric properties of $(1-x)BaZr_{0.2}Ti_{0.8}O_3$–$xBa_{0.7}Ca_{0.3}TiO_3$ thin films by sol–gel process, Appl. Surf. Sci. 388 (2016) 35–39.

[20] Y. Lin, G. Wu, N. Qin, D. Bao, Structure, dielectric, ferroelectric, and optical properties of $(1-x)Ba(Zr_{0.2}Ti_{0.8})O_3-x(Ba_{0.7}Ca_{0.3})TiO_3$ thin films prepared by sol–gel method, Thin Solid Films 520 (2012) 2800–2804.

[21] Q.G. Chi, H.F. Zhu, J.C. Xu, X. Wang, J.Q. Lin, Z. Sun, Y. Chen, Q.Q. Lei, Microstructures and electrical properties of $0.5(Ba_{0.7}Ca_{0.3})TiO_3$-$0.5Ba(Zr_{0.2}Ti_{0.8})O_3$ thin films prepared by a sol-gel route, Ceram Int. 39 (2013) 8195–8198.

[22] Q.G. Chi, C.H. Zhang, J. Sun, F.Y. Yang, X. Wang, Q.Q. Lei, Interface optimization and electrical properties of $0.5Ba(Zr_{0.2}Ti_{0.8})O_3-0.5(Ba_{0.7}Ca_{0.3})TiO_3$ thin films prepared by a sol−gel process, J. Phys. Chem. C 118 (2014) 15220–15225.

[23] Y. Chen, T.Y. Zhang, Q.G. Chi, J.Q. Lin, X. Wang, Q.Q. Lei, Low temperature growth of (100)-oriented $Ba(Zr_{0.2}Ti_{0.8})O_3$-$0.5(Ba_{0.7}Ca_{0.3})TiO_3$ thin films using a $LaNiO_3$ seed layer, J. Alloys Compd. 663 (2016) 818–822.

[24] B. Malič, A. Kupec, K. Vojisavljević, T. Pečnik, et al., Lead-Free Ferroelectric Thin Films, in: L. Klein (Ed.), Handbook of Sol-Gel Science and Technology, Springer International Publishing AG, 2016, p. 21.

[25] A. Jalalian, A.M. Grishin, X.L. Wang, Z.X. Cheng, S.X. Dou, Large piezoelectric coefficient and ferroelectric nanodomain switching in $Ba(Ti_{0.80}Zr_{0.20})O_3$-$0.5(Ba_{0.7}Ca_{0.3})TiO_3$ nanofibers and thin films, Appl. Phys. Lett. 104 (2014) 103112.

[26] S.R. Reddy, V.V.B. Prasad, S. Bysakh, V. Shanker, J. Joardar, S.K. Roy, Ferroelectric and piezoelectric properties of $Ba_{0.85}Ca_{0.15}Ti_{0.90}Zr_{0.10}O_3$ films in 200 nm thickness range, J. Am. Ceram. Soc. 102 (2018) 1277–1286.

[27] Z.-L. Cai, Z.-M. Wang, H.-H. Wang, Z.-X. Cheng, B.-W. Li, X.-L. Guo, H. Kimura, A. Kasahara, An investigation of the nanomechanical properties of $0.5Ba(Ti_{0.8}Zr_{0.2})O_3$–$0.5(Ba_{0.7}Ca_{0.3})TiO_3$ thin films, J. Am. Ceram. Soc. 98 (2015) 114–118.

[28] M. Sletnes, S.L. Skjærvø, M. Lindgren, T. Grande, M.-A. Einarsrud, Luminescent Eu^{3+}-doped $NaLa(WO_4)(MoO_4)$ and Ba_2CaMoO_6 prepared by the modified Pechini method, J. Sol-Gel Sci. Technol. 77 (2016) 136–144.

[29] A.B. Blichfeld, K. Bakken, D. Chernyshov, J. Glaum, T. Grande, M.-A. Einarsrud, Development of an experimental setup for high-temperature in situ studies of crystallization of thin films with atmosphere control, submitted to J. Synchrotron Rad. (2020).

[30] S. Gablenz, H.-P. Abicht, E. Pippel, O. Lichtenberger, J. Woltersdorf, New evidence for an oxycarbonate phase as an intermediate step in $BaTiO_3$ preparation, J. Europ. Ceram. Soc. 20 (2000) 1053–1060.

[31] P. Duran, D. Gutierrez, J. Tartaj, M.A. Banares, C. Moure, On the formation of an oxycarbonate intermediate phase in the synthesis of $BaTiO_3$ from (Ba,Ti)-polymeric organic precursors, J. Europ. Ceram. Soc. 22 (2002) 797–807.

[32] V. Ischenko, E. Pippel, R. Koferstein, H.-P. Abicht, J. Woltersdorf, Barium titanate via thermal decomposition of Ba,Ti-precursor complexes: the nature of the intermediate phases, Solid State Sci. 9 (2007) 21–26.

[33] V. Ischenko, J. Woltersdorf, E. Pippel, R. Köferstein, H.-P. Abicht, Formation of metastable calcite-type barium carbonate during low-temperature decomposition of (Ba,Ti)-precursor complexes, Solid State Sci. 9 (2007) 303–309.

[34] T.M. Raeder, K. Bakken, J. Glaum, M.A. Einarsrud, T. Grande, Enhanced in-plane ferroelectricity in $BaTiO_3$ thin films fabricated by aqueous chemical solution deposition, AIP Adv. 8 (2018) 105228.

[35] M. Shi, J. Zhong, R. Zuo, Y. Xu, L. Wang, H. Su, C. Gu, Effect of annealing processes on the structural and electrical properties of the lead-free thin films of $(Ba_{0.9}Ca_{0.1})(Ti_{0.9}Zr_{0.1})O_3$, J. Alloys Compd. 562 (2013) 116–122.

[36] G. Arlt, Twinning in Ferroelectric and Ferroelastic Ceramics – Stress Relief, J. Mat. Sci. 25 (1990) 2655–2666.

[37] V. Buscaglia, C.A. Randall, Size and scaling effects in barium titanate. An overview, J. Europ. Ceram. Soc. 40 (2020) 3744–3758.

[38] R. Sazinas, C. Bernuy-Lopez, M.-A. Einarsrud, T. Grande, Effect of CO_2 exposure on the chemical stability and mechanical properties of $BaZrO_3$-ceramics, J. Am. Ceram. Soc. 99 (2016) 3685–3695.

[39] R. Sažinas, I. Sakaguchi, I. Hasle, J.M. Polfus, R. Haugsrud, M.-A. Einarsrud, T. Grande, Tracer diffusion of ^{96}Zr and ^{134}Ba in polycrystalline $BaZrO_3$, Phys. Chem. Chem. Phys. 19 (2017) 21878.

[40] R. Sažinas, I. Sakaguchi, M.-A. Einarsrud, T. Grande, ^{134}Ba diffusion in polycrystalline $BaMO_3$ (M= Ti, Zr, Ce), AIP Advances 7 (2017) 115024.